

Synthetic control of actin polymerization and symmetry breaking in active protocells

Shiva Razavi^{1,2,*†}, Felix Wong^{3,4}, Bedri Abubaker-Sharif^{1,2}, Hideaki T. Matsabayashi^{2‡}, Hideki Nakamura^{2§}, Nhung Thi Hong Nguyen², Douglas N. Robinson^{2,5}, Baoyu Chen⁶, Pablo A. Iglesias^{1,2,7}, Takanari Inoue^{1,2*}

Nonlinear biomolecular interactions on membranes drive membrane remodeling crucial for biological processes including chemotaxis, cytokinesis, and endocytosis. The complexity of biomolecular interactions, their redundancy, and the importance of spatiotemporal context in membrane organization impede understanding of the physical principles governing membrane mechanics. Developing a minimal *in vitro* system that mimics molecular signaling and membrane remodeling while maintaining physiological fidelity poses a major challenge. Inspired by chemotaxis, we reconstructed chemically regulated actin polymerization inside vesicles, guiding membrane self-organization. An external, undirected chemical input induced directed actin polymerization and membrane deformation uncorrelated with upstream biochemical cues, suggesting symmetry breaking. A biophysical model incorporating actin dynamics and membrane mechanics proposes that uneven actin distributions cause nonlinear membrane deformations, consistent with experimental findings. This protocellular system illuminates the interplay between actin dynamics and membrane shape during symmetry breaking, offering insights into chemotaxis and other cell biological processes.

Copyright © 2024 The Authors, some rights reserved; exclusive licensee American Association for the Advancement of Science. No claim to original U.S. Government Works. Distributed under a Creative Commons Attribution NonCommercial License 4.0 (CC BY-NC).

INTRODUCTION

Originally used to study crystalline structures in physics (1), symmetry concepts have since expanded to encompass diverse realms of physics and living biological systems, reflecting a deeper understanding of the relationship between form and function (2–4). In biology, processes such as chemotaxis, cell division, phagocytosis, and cell-cell fusion are driven by actin polymerization–induced forces that move the plasma membrane in single cells (5–7). While the direction and magnitude of actin-generated forces vary among cellular processes, symmetry breaking, a phenomenon wherein a symmetric system exhibits directed behavior due to a bifurcation, serves as a unifying hallmark in these contexts (8–11). The asymmetric arrangement of actin cytoskeletal proteins can initiate spatial pattern formation, ultimately regulating cellular differentiation and development (12–14). Understanding how actin-induced asymmetries initiate and identifying their ramifications on cellular function are foundational challenges that warrant further investigation in biophysics and cell biology (3, 15, 16).

In eukaryotic cells, multiple regulatory mechanisms, including protein switches and allosteric regulation of signal transduction, are known to amplify biomolecular asymmetries (17, 18). To study

actin-induced symmetry breaking, *in vitro* reconstitution using simplified, membrane-bound systems devoid of cellular complexity has yielded insights into the regulatory mechanisms governing actin dynamics (19–22). Prior research has demonstrated that cell-sized vesicles, when subjected to polymerization of actin and other regulatory proteins, undergo membrane deformation due to forces exerted by filamentous F-actin (23–26). These studies revealed that symmetry could be broken if either capping protein (CP) or myosin was present (24, 27, 28). Although they have been informative, these experiments have been limited to cases where actin and its regulators were external to the vesicles and in effectively infinite supply. Further, work with encapsulated molecules (16, 28–31) has underscored the potential for cell-mimetic approaches that regulate reactions in space and time, inspiring the opportunities to perturb self-organization in confinement (32, 33).

Here, we present a synthetic platform enabling precise control of actin polymerization in giant unilamellar vesicles (GUVs) through chemical induction. Using chemical protein dimerization modules as dual sensing and actuation components, we demonstrate that rapamycin-triggered recruitment of a modified actin assembly-inducing protein (ActA), a robust actin-related protein 2/3 (Arp2/3) complex-dependent actin nucleation factor, to the inner GUV membrane activates the Arp2/3 complex, initiating actin polymerization and membrane force generation. Our platform effectively links biochemical cues to actin polymerization, demonstrating chemically induced symmetry breaking. This is manifested as local actin polymerization rates and GUV membrane deformations become asymmetric. Global administration of rapamycin lacking directional bias induces asymmetric actin distributions and membrane deformations in GUVs, revealing a lack of correlation with ActA distributions, which underscores symmetry breaking occurrence. Microscopic image analyses reveal that actin polymerization on the inner leaflets of GUVs leads to membrane deformations, inducing substantial shape eccentricity. Modeling the dynamics of actin polymerization within GUVs, we observe that the coupling of actin polymerization to asymmetrically

¹Department of Biomedical Engineering, Johns Hopkins University School of Medicine, Baltimore, MD 21205, USA. ²Department of Cell Biology, Center for Cell Dynamics, Johns Hopkins University School of Medicine, Baltimore, MD 21205, USA.

³Institute for Medical Engineering and Science, Department of Biological Engineering, Massachusetts Institute of Technology (MIT), Cambridge, MA 02139, USA. ⁴Infectious Disease and Microbiome Program, Broad Institute of MIT and Harvard, Cambridge, MA 02139, USA. ⁵Department of Chemical and Biomolecular Engineering, Johns Hopkins University, Baltimore, MD 21218, USA. ⁶Roy J. Carver Department of Biochemistry, Biophysics and Molecular Biology, Iowa State University, Ames, IA 50011, USA. ⁷Department of Electrical and Computer Engineering, Whiting School of Engineering, Johns Hopkins University, Baltimore, MD 21218, USA.

*Corresponding author. Email: srazavi@mit.edu (S.R.); jctinoue@jhm.edu (T.I.)
†Present address: Institute for Medical Engineering and Science, Department of Biological Engineering, MIT, Cambridge, MA 02139, USA.

‡Present address: Department of Mechanical Engineering, Tohoku University, Sendai, Miyagi 980-8579, Japan.

§Present address: Department of Synthetic Chemistry and Biological Chemistry, Kyoto University, Katsura, Kyoto 615-8530, Japan.

initiated nucleation sites align with the empirically observed spread of actin. Thin-shell modeling further suggests that observations of GUV shape eccentricity are qualitatively consistent with the mechanical deformations imparted by internal osmotic pressure, with the degree of actin asymmetry determining the extent of eccentricity. These findings showcase a synthetic biology platform and mechanistic model for regulating actin polymerization in GUVs. They provide insight into a tunable method for studying symmetry breaking in self-organization and elucidate the interplay among biological signaling, actin dynamics, and thin-shell mechanics in shaping cellular morphology (34).

RESULTS

Reconstituting chemically induced dimerization inside protocells enables external chemical sensing

We aimed to develop a platform that enables precise control of actin polymerization and membrane remodeling in protocells, triggered by external chemical cues. This was achieved by designing a protein dimerization-based sensing and actuation module encapsulated within GUVs (fig. S1). We adopted chemically inducible dimerization (CID) based on FK506 binding proteins (FKBPs) and FKBP-rapamycin binding domain (FRB), which heterodimerize in the presence of a small molecule derived from rapamycin. CID has been extensively applied in cellular contexts to manipulate biochemical reactions on the surface of membranes (35), tether artificial membranes (36), and mediate phase separation in emulsion (37), prompting us to explore its application in protocells.

We first linked FRB and FKBP, each to cyan and yellow fluorescent proteins, respectively (6xHis-CFP-FRB and 6xHis-YFP-FKBP). We encapsulated purified forms of these proteins, each at a concentration of 3.2 μ M, inside GUVs consisting of lipid membranes derived from eggs' phosphatidylcholine. These GUVs were generated using the inverted emulsion technique (Methods) (38–41). We found that stimulating the GUVs with an external, undirected supply of rapamycin

resulted in heterodimerization of the FKBP and FRB proteins, as indicated by Förster resonance energy transfer (FRET) measurements of CFP. Heterodimerization induced by rapamycin was detected within minutes, showing a more robust performance at 100 μ M rapamycin compared to lower concentrations (fig. S1), consistent with the concentration range previously reported for in vitro studies (42, 43). In contrast, administration of vehicle [dimethyl sulfoxide (DMSO)] did not result in FRET signal intensity increase, indicating no heterodimerization (fig. S1). These findings confirm that our engineered CID modules enable externally-triggered signal processing within GUVs.

To achieve a membrane-localized output, we subsequently aimed to engineer rapamycin-induced localization of the luminal CFP-FRB toward the membrane-anchored FKBP (Fig. 1A). To this end, we coupled FKBP to the effector domains of the myristoylated alanine-rich kinase substrate (MARCKS-ED), a positively charged peptide that binds to phosphatidylserine (PS) (44). The resulting construct, mCherry-FKBP-MARCKS, was purified and co-encapsulated with purified CFP-FRB inside PS-containing GUVs (table S1). We further verified that MARCKS exhibits no affinity for PC lipids (fig. S2), reaffirming our selection of PS lipids for this experiment. With this design, we localized mCherry-FKBP-MARCKS at the membrane while retaining the luminal distribution of FRB (Fig. 1B). Upon rapamycin administration, the luminal CFP-FRB localized to the membrane (Fig. 1, B and C, and movie S1) within minutes, a timescale similar to that previously observed with CID in mammalian cells (45). The minute-scale temporal dynamics of our GUV-encapsulated CID system highlight its ability to recapitulate the temporal dynamics of actin in its native cellular context.

External chemical sensing supports on-demand actin polymerization inside the protocells

We then conjugated our CID-based constructs, tailored for GUV membranes, with actin polymerization. Specifically, we fused FRB to a reengineered domain of the actin assembly-inducing protein ActA (1–183) (fig. S3). ActA is a potent Arp2/3-dependent actin nucleation

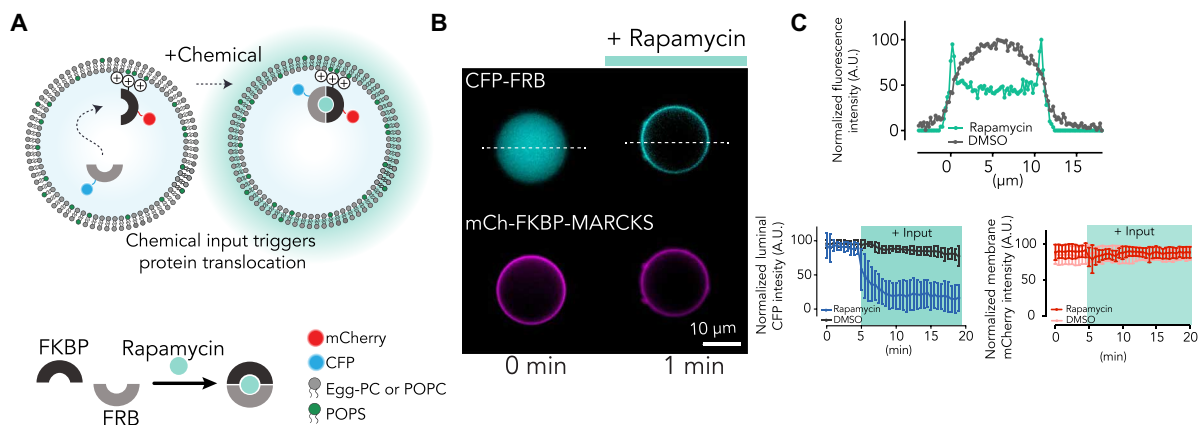


Fig. 1. Reconstitution of actuation inside protocells. (A) Schematic of the GUVs containing the membrane-anchored mCh-FKBP-MARCKS and luminal CFP-FRB proteins. Rapamycin-induced dimerization of FKBP and FRB moves the CFP-FRB protein toward the membrane. (B) Epi-fluorescence images of CFP-FRB (4.4 μ M) and mCh-FKBP-MARCKS (7.8 μ M) in the symmetric GUVs containing 1-palmitoyl-2-oleoyl-glycero-3-phosphocholine:1-palmitoyl-2-oleoyl-sn-glycero-3-phospho-L-serine (POPC:POPS) (4:1 mol %) in the inner lipid leaflet. The initially luminal CFP-FRB protein switches localization to the membrane within minutes after rapamycin administration. (C) Line scans of the mCherry and CFP fluorescence intensity across the vesicle show protein localization before and after rapamycin addition (top). The luminal fluorescence intensity of the CFP-FRB (bottom) normalized by the average of the initial values before rapamycin treatment is plotted, highlighting the minute-scale CFP-FRB translocation toward the membrane only in the presence of rapamycin but not DMSO vehicle. The mCherry signal associated with the membrane marker remains membrane-localized throughout the experiment. $n = 14$ from three independent experiments for both rapamycin and DMSO conditions. Error bars represent SD. The green box marks rapamycin presence. A.U., arbitrary units.

promoting factor (46, 47) that we recently engineered to generate forces on the cytoplasmic membranes of mammalian cells (48). Given the nonspecific affinity of our purified ActA for PS lipids, we used a histidine-nickel affinity approach for membrane anchoring rather than relying on electrostatic interactions. We encapsulated purified forms of the C-terminal 2xStrep affinity-tagged ActA-FRB construct (2xStrep-ActA-FRB-CFP) together with the Arp2/3 complex, G-actin (mixed with 8% Alexa Fluor 488-labeled G-actin for visualization), 6xHis-tagged mCherry-FKBP, and adenosine 5'-triphosphate (ATP) inside GUVs containing nickel-conjugated lipids to enable membrane anchoring of the His-tagged FKBP. We also added polyethylene glycol-phosphatidylethanolamine (PEG-PE) to the membrane mix to minimize protein-membrane interactions (Fig. 2, A and B, and Table 1).

In this design, initially, all components except for membrane-bound mCherry-FKBP were located within the luminal body. Upon the administration of rapamycin to the external environment, we observed redistribution of the engineered ActA to the membrane, activating the Arp2/3 complex, as confirmed by actin assembly measurements performed in the test tube (fig. S4). Subsequently, stochastic and asymmetric patches of actin emerged on the membrane and grew to engulf the GUV boundary (Fig. 2B and movie S2). With sufficiently high concentrations of G-actin (~3 μ M), actin polymerization on the membrane deformed GUVs smaller than ~50 μ m in diameter (Fig. 2B).

To validate that membrane deformations emerge as a result of actin assembly, we externally administered latrunculin A, a toxin that depolymerizes F-actin, binds G-actin, and hinders actin assembly (49). With latrunculin A present in the media, we found that actin patches failed to grow; additionally, the fluorescence intensities of already-developed F-actin patches decreased over time (fig. S5). These results indicate that actin growth was caused by actin polymerization, rather than the accumulation of monomeric G-actin. Without ActA or Arp2/3, actin failed to polymerize. In the absence of rapamycin, we found that only a baseline level of background luminal actin polymerization occurred (Fig. 2C and figs. S6 and S7). These observations suggest that a threshold concentration of ActA drives actin polymerization, a finding resembling previous results indicating that the WASP family of Arp2/3 activators (50) also exhibits a concentration threshold for downstream Arp2/3 activation. Notably, our rapamycin-inducible modulation of a threshold-dependent signaling cascade, resulting in actin polymerization, offers a system capable of investigating biological symmetry breaking with minimal regulatory components.

Actin polymerization is dynamic and exhibits symmetry breaking

To quantify the dynamics of actin polymerization in our model system, we generated kymographs for the spatial distributions of ActA and actin fluorescence intensities, as well as membrane curvature, as functions of time (Fig. 3A, Methods, and the Supplementary Materials).

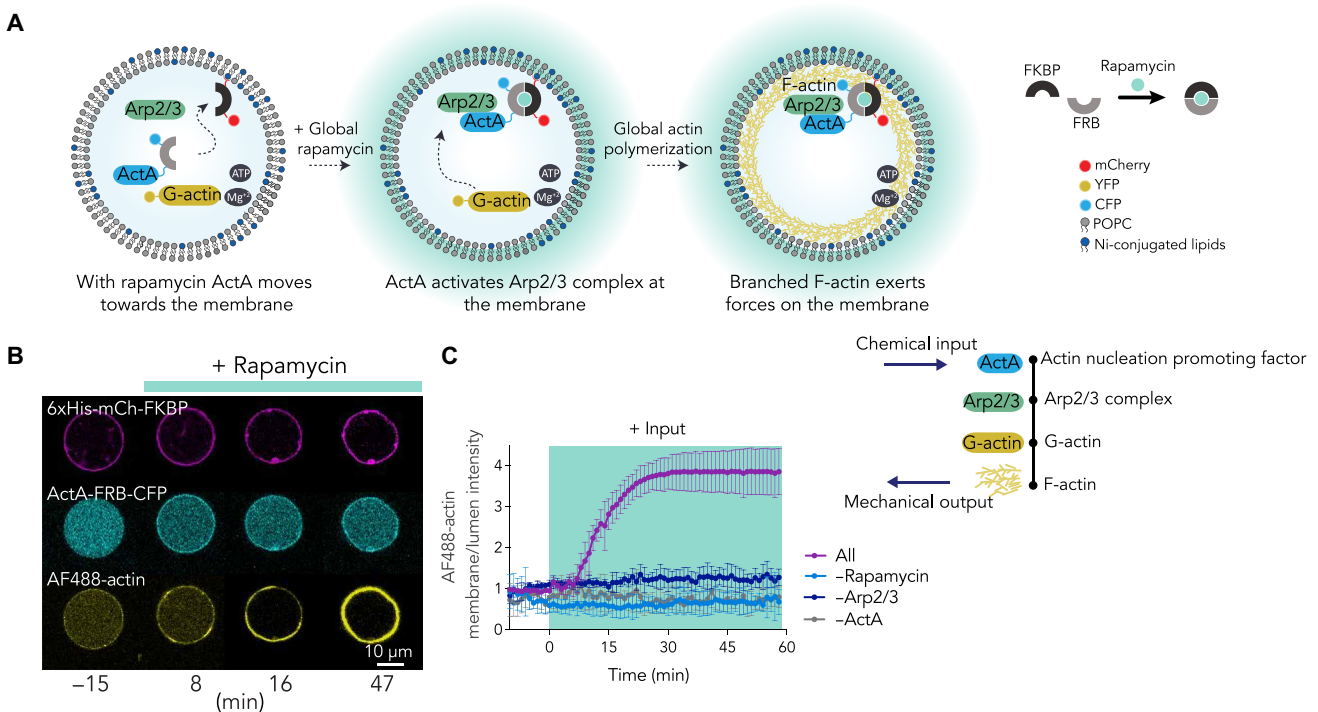


Fig. 2. Reconstitution of actin-induced force generation inside rapamycin sensing active protocell. (A) Schematic of the signaling pathway. ActA activates Arp2/3 complex on the membrane, where F-actin branches grow to generate force. CID system modules coupled with ActA (1–183) transduce rapamycin sensing to force actuation. ActA (1–183)-FRB-CFP, Arp2/3, and G-actin are initially diffuse in the lumen. mCherry-FKBP is anchored at the membrane. (B) Confocal images of symmetric POPC:1,2-dioleoyl-sn-glycero-3-[(N-(5-amino-1-carboxypentyl)iminodiacetic acid)succinyl](nickel salt) [DGS-NTA(Ni)]:PEG-PE (95:4:1) GUVs containing 6xHis-mCh-FKBP, ActA (1–183)-FRB-CFP (2 μ M), Arp2/3 (150 nM), G-actin (3 μ M), and ATP (1 mM) in Mg²⁺ buffer. All protein constructs except 6xHis-mCh-FKBP are luminal at $t = 0$. With rapamycin, ActA accumulated on the membrane and triggers F-actin forces. AF488, Alexa Fluor 488. (C) Time course of mean actin localization in the presence of rapamycin and all components of the signaling cascade, as well as negative controls where Arp2/3, ActA, or rapamycin is absent. From three independent experiments, $n = 6$ for All, $n = 4$ for -Arp2/3, $n = 9$ for -ActA, and $n = 10$ for DMSO conditions. Error bars indicate SDs. Green area marks rapamycin presence.

Table 1. Molecular constituents of protocells.

	Part	Function	Concentration
Protein network	6xHis-mCherry-FKBP	Chemical sensing: membrane anchoring	9.5 μ M
	ActA-FRB-CFP	Chemical sensing: Arp2/3 activation	2 to 8.5 μ M
	Arp2/3 complex	Actin nucleation	0.15 to 0.5 μ M
	G-actin	Force generation	1.5 to 3 μ M
Lipids	POPC	Biological membrane mimic anchoring	94 mol %
	DGS-NTA(Ni)	Sensory modules	5 mol %
	PEG	Reducing unspecific lipid protein interaction	1 mol %
Inner buffer	ATP	Energy source	1 mM
	MgCl ₂	Actin stability and polymerization	<1 mM
	KCl	Physiological salt	<50 mM
	Tris-HCl (pH 7.5)	pH stability	>10 mM
	Sucrose	Osmotic pressure balance	850 mM

The kymographs revealed that, in typical GUVs, ActA and actin were uniformly distributed in space until ~5 min after rapamycin administration (designated as $t = 0$), after which discrete actin nucleation sites appeared on the membrane surfaces. The resulting actin polymerization generated forces that caused the contraction of the membrane, evident through the heightened intensity of the membrane marker (Fig. 3A). Principal components analyses further showed that multiple discrete peaks in the actin and local curvature kymographs and, to a substantially lesser extent, in the ActA kymographs accounted for most of the empirically observed variation across GUVs (fig. S8). To investigate whether the heterogeneity of actin nucleation was associated with upstream ActA distribution, we calculated ActA-actin correlations for each of 18 GUVs across time (Fig. 3B). These analyses indicated a small ActA-actin correlation of ~0.2, which likely arose from lipid artifacts in the membrane where proteins appeared enriched. These correlations remained unchanged after the addition of rapamycin. However, discrete and asymmetric actin nucleation occurred after rapamycin addition, as supported by plots of actin fluorescence intensity along the GUV contours (Fig. 3C). The absence of correlation increase with respect to ActA suggests that the symmetry breaking is spontaneous and independent of detectable levels of ActA, consistent with observations from previous studies on symmetry breaking (51).

We next performed similar correlation analyses for membrane curvature (Fig. 3B). This assessment highlighted that ActA and actin were essentially uncorrelated with membrane curvature, despite a small increase in correlation from -0.2 to 0 after rapamycin addition for ActA and curvature (Fig. 3B). While actin polymerization may lead to local membrane deformations, it is possible that these deformations may manifest in membrane curvature alterations on a global scale. To investigate this hypothesis further, we quantified the entropy as a global measure of variation, reflecting changes in the distributions of values, such that higher entropy values indicate higher asymmetry, across all points on the GUV contours (Fig. 3, C and D). We calculated the entropy for ActA intensity and actin intensity; additionally, we calculated the eccentricity of the best-fitting ellipse to each GUV

contour as a global measure of shape eccentricity. We found that, in contrast to ActA entropy, the actin entropy and eccentricity persistently increased after rapamycin addition. Furthermore, the range of eccentricity distribution appeared to be directly influenced by the experimental condition (figs. S6 and S7). This finding was corroborated by a Kolmogorov-Smirnov test, which revealed a statistically significant shift ($P < 0.0001$) in the measured eccentricity range exclusively within the experimental condition where all proteins and rapamycin were present, while none of the negative controls exhibited such a shift (fig. S6 and Methods). These results are consistent with our observations that actin nucleation is asymmetric and uncorrelated with ActA (Fig. 3, B and D) and further suggest that asymmetry in the actin distribution is associated with global, but not local, GUV shape changes.

While we have focused on the correlations between ActA, actin, and curvature for each GUV, these correlations may differ globally across GUVs. To investigate this possibility, we computed ActA and actin mean intensity profiles at representative time points before and after rapamycin treatment (Fig. 3E). Intriguingly, and akin to our previous analyses (Fig. 3B), we found no correlation between the mean intensities of ActA and actin after rapamycin treatment, despite the two quantities being moderately positively correlated, possibly due to initial lipid artifacts in the membranes, before rapamycin treatment. Correlations between mean ActA intensity and eccentricity were weaker, while mean actin intensity was uncorrelated with eccentricity before rapamycin treatment. The strongest correlation, of ~0.55, emerged between mean actin intensity and eccentricity after rapamycin treatment, again indicating that increased actin polymerization is associated with asymmetric GUV shapes. Together, these results further highlight symmetry breaking in actin polymerization and GUV shape in our synthetic platform.

Actin polymerization is associated with GUV shrinkage and shape eccentricity

As our analyses indicate that asymmetric actin polymerization is associated with changes in GUV shape, we further investigated the dynamical and mechanical implications of actin symmetry breaking.

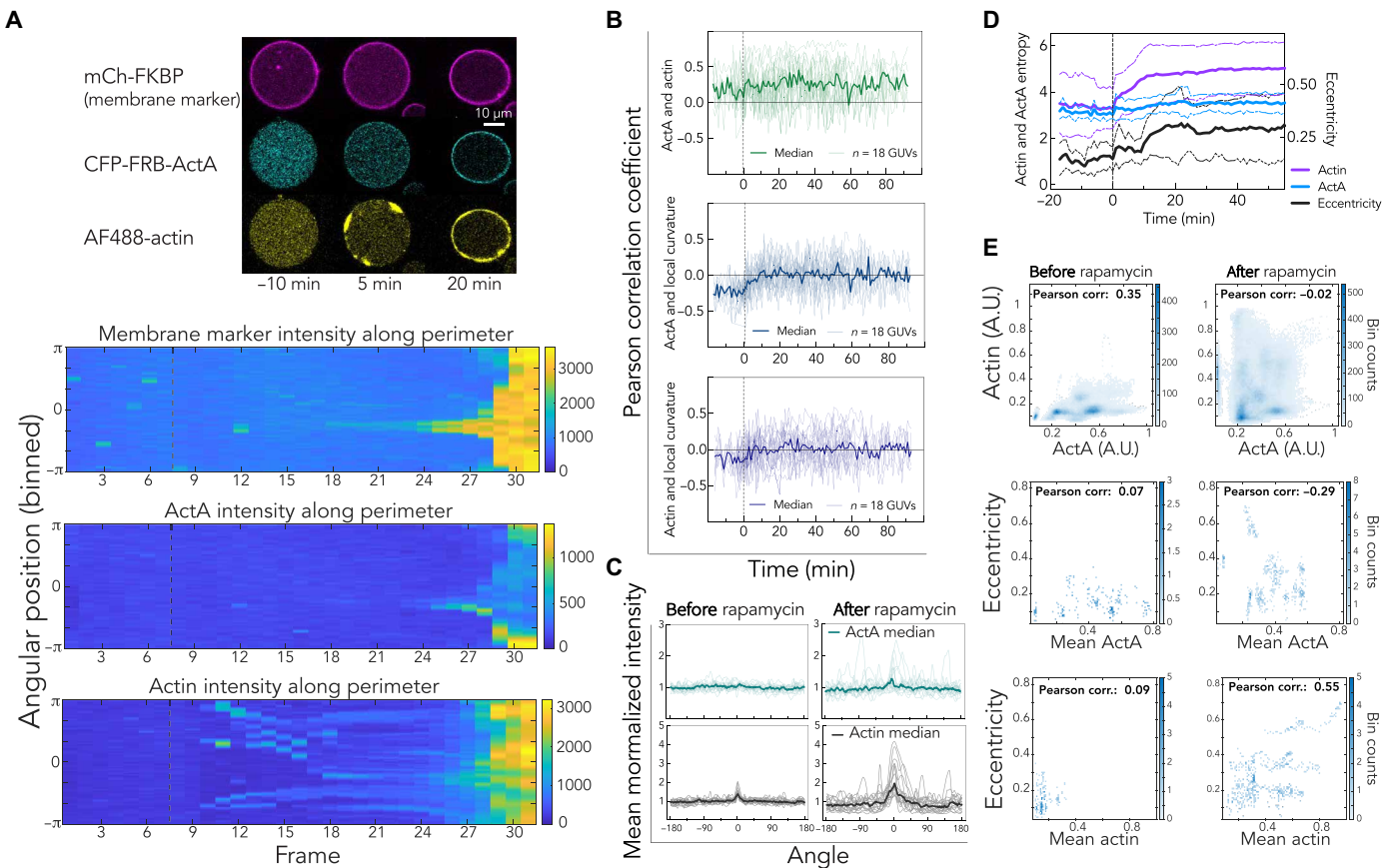


Fig. 3. Symmetry breaking in biochemical and physical spaces on a local and global scale. (A) Representative confocal image of a GUV before and after rapamycin addition together with its corresponding kymographs tracking enrichment of ActA and actin on the membrane in time. $t = 0$ represents the rapamycin addition time point. (B) Tracking the Pearson correlation coefficient between biochemical parameters (ActA and actin) over time highlights no correlation change upon rapamycin addition (top). The Pearson correlation coefficient evolution for ActA and local curvature become further decorrelated upon rapamycin addition (middle). Similarly for actin and local curvature, no correlation is observed (bottom). (C) Mean-normalized fluorescence intensity profiles of ActA and actin shown at two frames before rapamycin and 10 frames after rapamycin addition. (D) Plots of the entropy of boundary parameters over time, highlighting that ActA entropy remains steady, while those of actin and eccentricity both spike after rapamycin addition. Error bars indicate SD. (E) Plots of mean ActA intensity, mean actin intensity, and eccentricity, where the bulk correlation is computed over aggregated data from all GUVs for 18 frames before rapamycin and 35 frames after rapamycin input. For each plot, $n = 18$ from three independent experiments. The dashed black line marks the input addition time point. Images are captured at the frequency of one frame per minute.

Building on our observations of actin fluorescence at the GUV surface across all time points, we assumed that a spherical, linear-elastic, and isotropic thin-shell layer of actin is initially anchored to the inner leaflet of each GUV and that the membrane surface area is larger than that of the actin shell's. Within our system, the osmolarity of the inner solution was determined to be 1633 mOsmol/kg, while that of the outer solution was 1298 mOsmol/kg (Methods). As internal, outward turgor pressure on the order of ~ 0.1 to 1 atm can be generated by the millimolar-scale osmotic imbalance of solutes across the GUV (Table 1), thin actin shell is the main load bearing element and will be remodeled by additional actin polymerization (Fig. 4A).

Previous studies have assumed that the actin polymerization rate outside a droplet, with actin polymerization occurring in one direction, depends on the normal stress in the droplet with a Kramer's rate dependence (52). Here, building on this assumption of mechanical stress-dependent actin polymerization, we assume that the local, volumetric rate of actin polymerization (dV/dt) at any surface coordinate (θ, ϕ) and at time t depends on the in-plane mechanical

stress, $\sigma(\theta, \phi, t)$, with a Kramer's rate: $dV(\theta, \phi, t)/dt = \ell^3 v_0 e^{\sigma(\theta, \phi, t)/\sigma_0}$, where σ_0 is a baseline value of stress, ℓ is the length of an actin monomer, and v_0 is a unit rate of actin polymerization. For a spherical actin shell, the nonvanishing in-plane stresses are $\sigma_0 = pr_0/2h_0$, where p is the turgor pressure, r_0 is the shell radius, and h_0 is the initial actin shell thickness. Anticipating that ActA-dependent actin polymerization results in the local shell thickness being multiplied by a factor of $f \gg 1$, we expect that the ActA-enriched regions with highest mechanical stress are at the leading edges; this is confirmed by finite-element simulations of pressurized spherical shells with two different thicknesses (Fig. 4B and Supplementary Materials). When actin finishes polymerizing laterally across the GUV surface at time t^i , the stresses are approximately homogeneous and the form of dV/dt suggests that actin thickens linearly in time. Detailed calculations for this model (Supplementary Materials) predict that

$$c(t) \sim \cos^{-1} 1 - \frac{\ell^2 v_0 e^f t}{r_0^2} (t < t^i), h(t) \sim t (t \geq t^i), r(t) \sim 1/t (t \geq t^i) \quad (1)$$

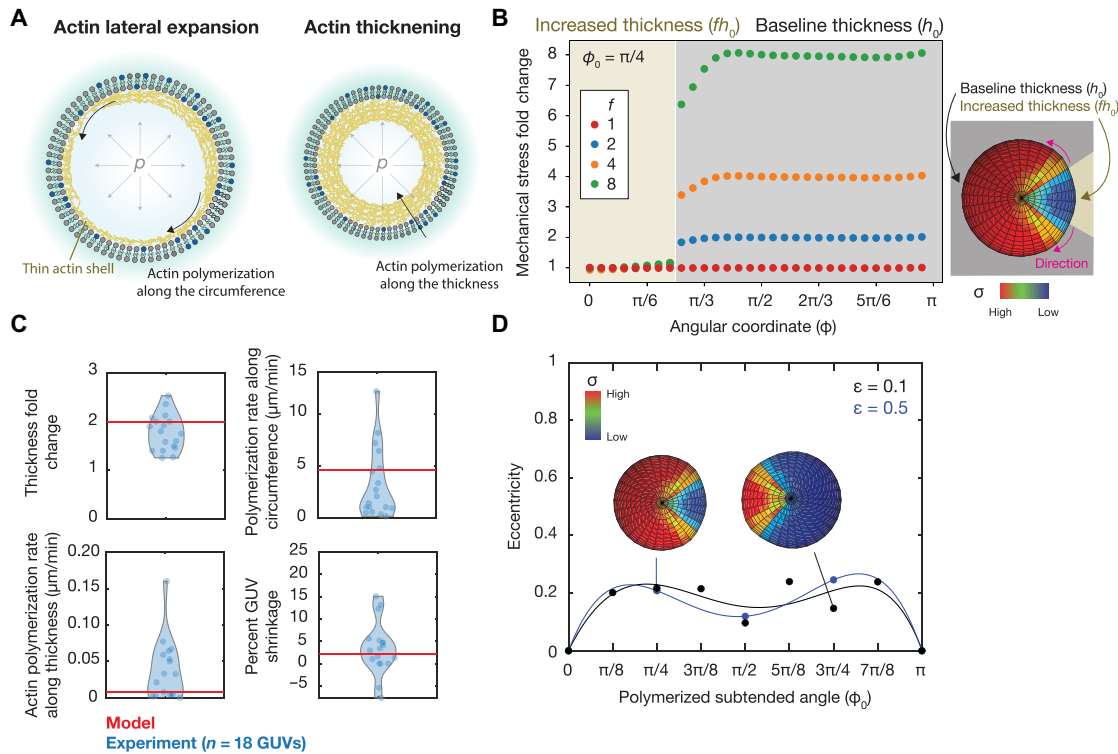


Fig. 4. Biophysical modeling of the dynamics and mechanics of actin polymerization. (A) Schematic of actin dynamics predicted by the model, in which the volumetric rate of actin polymerization depends on the mechanical stress. Actin polymerization is predicted to predominantly occur along the circumference (lateral expansion) and then along the GUV thickness (thickening). The actin is viewed as a thin elastic shell loaded by the internal turgor pressure, p . (B) Plot of the fold change in mechanical stress, $\sigma(\phi)/\sigma_0$, where $\sigma(\phi)$ is the average maximum principal stress at the angular coordinate ϕ and $\sigma_0 = pr_0/2h_0$ is the principal stress where the thickness is h_0 . Results are shown for a polymerized subtended angle of $\phi_0 = \pi/4$ and different thickness factors of $f = 1, 2, 4$, and 8. Inset: Representative finite-element simulation results. The maximum principal stress is visualized. (C) Comparison of model predictions (red lines) with experimental measurements (blue points) for the 18 GUVs analyzed in Fig. 3, for characteristic parameter values of $h_0 = 0.1 \mu\text{m}$, $f = 2$, $\epsilon = 0.1 \mu\text{m}$, $r_0 = 10 \mu\text{m}$, $v_0 = 200 \text{ min}^{-1}$, actin elastic modulus $E = 0.1 \text{ GPa}$ (66, 67), actin Poisson's ratio $\nu = 0$, and turgor pressure $p = 1 \text{ atm}$. Rates were calculated as linear approximations; see the Supplementary Materials for details. (D) Plot of simulated GUV eccentricity values as a function of the polymerized subtended angle, ϕ_0 , for the same parameter values as in (C), corresponding to mechanical strains of $pr_0/Eh_0 = 0.1$ (black). A value of $p = 5 \text{ atm}$ was also used in the simulations, corresponding to mechanical strains of 0.5 (blue).

where $c(t)$ is the fraction of the shell circumference at which ActA-dependent actin polymerization has already occurred at time t , h is the polymerized thickness of the actin shell at time t , and r is the radius of the actin shell at time t , which decreases due to shell thickening counteracting the turgor pressure and decreasing the mechanical strain, ϵ , in the actin shell (Supplementary Materials). For characteristic values of all other parameters, fitting the unit actin polymerization rate (v_0) predicts both the quantitative rates of actin's lateral expansion and thickening, and we find that these rates and the resulting shrinkage of the actin shell are consistent with our empirical observations (Fig. 4C). Furthermore, quantifying the magnitude of GUV shrinkage toward the end of our time lapses reveals a radial shrinkage on the order of $\sim 5\%$, consistent with our model predictions (Fig. 4C).

The consistency between our empirical observations and our biophysical model, therefore, suggests that asymmetric actin polymerization is a dynamical process that results in mechanical alterations to GUVs. Moreover, at long timescales, actin thickening can result in GUV actuation. Given that actin symmetry breaking was also associated with shape eccentricity (Fig. 3D), we further investigated whether mechanical deformations could give rise to substantial shape eccentricity. For simplicity, we modeled actin as a shell with two thicknesses,

using finite-element simulations across a range of angles subtended by the thicker actin (Fig. 4D). We found that, for finite values of mechanical strain and across a broad range of shell thicknesses, the shape of the simulated actin shell was eccentric and could be fit by ellipsoids with eccentricity values on the order of ~ 0.2 (Fig. 4D), consistent with the magnitude of eccentricity values inferred from experiments (Fig. 3D). These results indicate that shape asymmetry can arise as a mechanical consequence of actin symmetry breaking alone.

Asymmetric inputs validate timescales and elucidate the origins of symmetry breaking

To further probe our system, we reduced its spatial degrees of freedom by constraining the position of the rapamycin input. We induced a rapamycin gradient on the length-scale of a GUV using a point source by administering ethanol-solubilized rapamycin with a microinjector close to each GUV and adding Alexa Fluor 647 dye to track the rapamycin gradient [as its Stokes radius is comparable to that of rapamycin (53)]. Initial experiments with POPC lipids highlighted fast actin spreading around the GUV hampering a local response (fig. S9). To confine the localization further, we used deformable DPPC lipids, which exhibit lower lateral diffusion and membrane

fluidity compared to POPC lipids, yet still deform upon actin polymerization (fig. S10 and table S1) (54). In addition, with all other conditions held constant, we reduced the ActA concentration to limit its availability (Fig. 5A and table S2). After administering rapamycin locally, we observed that ActA always translocated toward the membrane region proximal to the needle tip, and, within ~5 min, ActA decorated the entire GUV membrane. Furthermore, we found that subtle but stable ActA localization at the needle tip, on the order of ~1 min, was sufficient to bias an actin nucleation site to appear at the same site. These observations are consistent with the actin nucleation dynamics observed in an *in vitro* pyrene assay (fig. S4). Intriguingly, transient ActA leading to stable actin accumulation is reminiscent of memory behavior due to time delay (55), and these observations indicate that ActA may store positional information downstream of the local amplification potentially mediated by the Arp2/3 complex (fig. S11).

Downstream of transient ActA localization, we found that, within ~15 min, by which time the ActA distribution appeared uniform across the membrane, F-actin patches emerged next to the needle tip and grew to encompass ~85% of the membrane (Fig. 5, B and C, and movie S3). These patches expanded laterally and in thickness similar to our previous experiments, in which rapamycin was administered without a directional bias. These results show that asymmetric actin polymerization is uncorrelated with ActA irrespective of the route (undirected or directed) of rapamycin induction. As in the previous experiments, substantial shape eccentricity and membrane shrinkage also occurred, consistent with our model predictions (Fig. 4D). Additional perturbations support that actin symmetry breaking is associated with local fluctuations in rapamycin concentration and that actin polymerization is required for membrane shape deformations: When we altered the needle placement in independent experiments, we observed a positive correlation between the needle tip and actin polymerization initiation sites. This manipulation ruled out the possibility of flow-based interference or phase-separated lipids driving the local output (Fig. 5, C and D, and fig. S11) and further suggested that local, nonequilibrium fluctuations in rapamycin concentration, which may result in small ActA fluctuations not seen in our correlation analyses, are associated with actin symmetry breaking (Fig. 5E). Consistent with this hypothesis, we found enhanced localization of F-actin after increasing the GUV

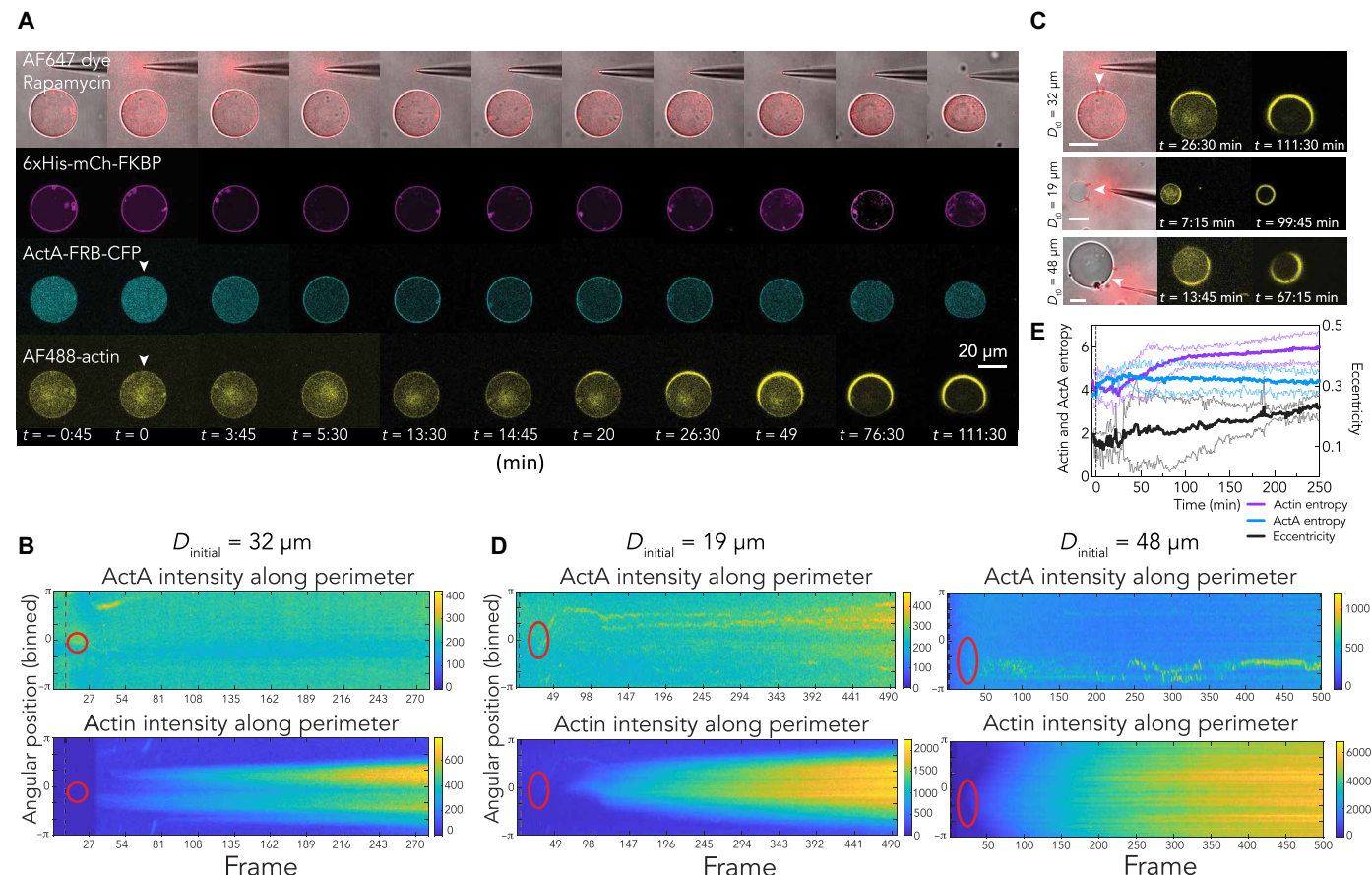


Fig. 5. Reconstitution of spatially controlled localized actin deformation. (A) Confocal images of GUVs during rapamycin administration. Upon rapamycin release (marked by the pink Alexa Fluor 647 dye signal), ActA first translocates to the location marked by the white arrow. Local F-actin appears at the same site within ~15 min. (B) Kymographs showing the evolution of the ActA and actin signal intensity on the membrane for the GUV presented in (A). The red oval marks the effective high rapamycin concentration area. (C) Comparison of the actin thickening versus spreading, for GUVs of different radii. The area between the two lines highlights the effective rapamycin area. Scale bars, 20 μm . (D) Similar to (B) but showing a kymograph of the signal accumulation for the 48- and 19- μm GUVs depicted in (C). Time 0 corresponds to the rapamycin input addition. (E) Plots of the entropy of boundary parameters over time, highlighting that ActA entropy remains steady, while that of actin and eccentricity both spike after rapamycin addition. Error bars indicate SD. The dashed black line marks the input addition time point. Images are captured at the frequency of one frame per minute.

diameter size, suggesting that symmetry breaking is length-scale dependent (Fig. 5, B to D, and figs. S12 and S13). To determine the radial rate of actin polymerization, we analyzed the slope of the actin kymographs (fig. S14 and Methods). Our observations revealed that the polymerization rate correlates with the size of the GUVs, occurring more rapidly in smaller ones. In addition, the distinction between local and global input influences the number of actin peaks that emerge. For larger GUVs, the relatively large membrane surface adjacent to the needle likely depletes the reaction substrate and serves as an internal nonmolecular inhibitory element.

We last investigated the factors influencing actin thickening and GUV shape deformations (Fig. 5D). To assess whether we can sculpt this thickening by integrating additional actin modulators, we used a purified CP, Cap32/34, which binds the barbed end of actin, preventing actin monomer addition or loss. In the presence of 100 nM of purified Cap32/34 (56), we found that actin patches became sparse and thin and eventually disintegrated. This indicated that actin polymerization at barbed ends supported actin thickening, consistent with bulk actin polymerization assay measurements (fig. S4), in which actin polymerization was inhibited with overloaded Cap32/34 (3 μM; fig. S15). Moreover, addition of cofilin, which promotes actin disassembly in conjunction with Cap32/34, abolished actin thickening in response to local administration of rapamycin. With Cap32/34 at a relatively low concentration (50 nM), we did not observe membrane protrusion or invagination even in the presence of higher concentrations of G-actin (fig. S15), suggesting that shape deformations were bottlenecked by actin polymerization. Together, these results suggest that the timescale of ActA stability is critical to achieving a stable actin polymerization output and that actin polymerization is needed for shape deformations. In addition, these experiments further suggest that symmetry breaking is associated with local fluctuations in rapamycin concentration.

DISCUSSION

In vitro cell mimetic systems aim to assemble the minimal set of protein and lipid modules to output a desired function. Here, we have developed a cell mimetic platform that implements spatio-temporal control modules to achieve biological symmetry breaking with actin. To our knowledge, our platform comprises the most reduced network of biological nodes that can produce symmetry breaking in a context relevant to diverse physiological processes, including chemotaxis. Specifically, our design is devoid of CP, myosin, or phase-separated lipids that were previously considered indispensable to symmetry breaking (24, 57, 58). Using our synthetic platform, we have found that the application of undirected external chemical inputs results in directed actin polymerization and asymmetric membrane deformations. The actin polymerization and shape deformations are uncorrelated with upstream biochemical cues, indicating biological symmetry breaking. Biophysical modeling suggests that a model of actin polymerization aligns with our experimental observations and can lead to substantive membrane shape changes through mechanical deformations. Local experiments, in which rapamycin is directionally administered, further confirm these dynamics and suggest that actin symmetry breaking arises from local fluctuations in rapamycin concentration.

Our study demonstrates that signal amplification from upstream chemical components, such as Arp2/3, to actin is adequate to induce symmetry breaking. Moreover, our platform exemplifies how

implementing CID in an active model system can lead to changes in the system's mechanical and morphological properties. We observed that second-long local ActA enrichment on the membrane close to the input was sufficient to bias the F-actin toward the input source, a finding that points to the potential positive feedback characteristic of actin polymerization in response to ActA-induced Arp2/3 activation (59). Further investigations using Arp2/3 mutant variants could provide more precise control over symmetry breaking. Although challenging, obtaining higher-resolution structural information of the Arp2/3 and actin molecules inside GUVs could guide mechanisms of activation in a membrane context (60).

Our biophysical modeling of the dynamics and mechanics of actin polymerization underscores the interplay between actin symmetry breaking and GUV shape deformations. Other models have been developed to describe actin dynamics and mechanics in other contexts; notably, these models have focused on different aspects of actin polymerization, including actin flow (25) and settings of reduced dimensionality (52). The model developed in this work is specific to our platform in that it focuses on the patterns of actin polymerization generated through CID, as well as the stretching deformations caused by internal osmotic pressure. Our model suggests that the mechanical stress-dependent incorporation of actin subunits at actin nucleation sites is consistent with our empirical observations and that the coupling of asymmetric actin patterning with thin-shell mechanical properties alone can generate asymmetric GUV shapes. Our model and its conclusions may generalize beyond our experimental platform to offer physical insights into other processes, including actin-dependent cell shape changes and cell motility.

In general, bottom-up approaches that rely on *de novo* assembly to understand biophysical principles have recently gained traction in synthetic biology. Our work exemplifies these efforts on the molecular scale. The presented platform provides insight on the spatiotemporal localization of the molecular components and elucidates the design principles governing chemical signaling, actin assembly, and symmetry breaking. Our platform offers a previously unknown GUV manipulation technique (61, 62) and a versatile imaging pipeline to track the locality-specific concentration of biomolecules in a dynamic GUV over time, complementing other realized modalities (63, 64). Our image processing and statistical analysis scheme enables probing the biomolecular and geometric features of symmetry breaking, a pipeline that is applicable to other GUV- and cell-based studies. By combining experiment and modeling, our results offer the ability to better understand macroscopic cellular processes, including morphogenesis, motility, and division, that build on fundamental biophysical and active matter principles to accomplish complex biological tasks.

METHODS

DNA plasmid construction and protein purification

DNA plasmid construction and protein purification are detailed in the Supplementary Materials and DNA Sequence Files deposited at DOI: 10.5061/dryad.rxwdbryh9.

GUV fabrication

GUVs were prepared adopting our previously reported protocol (39, 40). Lipids were purchased from Avanti in their chloroform-solubilized form and were aliquoted with a glass Pasteur pipette to achieve the desired final molar concentrations. The lipids underwent vacuum drying overnight. Except for Egg-PC lipids, which were dissolved in

mineral oil, all other lipids were dissolved in hexadecane at a concentration of 1 mg/ml in a Hybaid HS9320 rotisserie hybridization oven, maintaining a temperature of at least 65°C, depending on the lipid's transition temperature. To assemble the GUVs, 300 μ l of the outer GUV solution was placed in a test tube, and 300 μ l of the room temperature lipid mixture containing the outer leaflet was gently pipetted on top. The two layers were left undisturbed for 10 to 15 min. The inner leaflet lipid mix, identical to the outer leaflet in our case, was combined with 100 μ l of the droplet containing the desired GUV content. This mixture was vigorously tapped to achieve a homogenous turbid emulsion phase, which was then gently pipetted into the test tube to form the third layer. Following centrifugation at 2500g for 7 min, the bottom of the tube was punctured with a needle to collect the bottom-most layer containing GUVs floating in the outer solution. The osmolarities of the inner and outer GUV buffer were measured with a Gonotec Osmomat 3000.

Global CID-based protein translocation in GUVs

For CFP-FRB translocation toward the mCherry-FKBP-MARCKS-bound membrane, we reconstituted 4.4 μ M FRB-containing and 7.8 μ M FKBP-containing constructs in phosphate-buffered saline (PBS) buffer inside symmetric GUVs (table S1) using the inverted emulsion-based GUV fabrication technique previously reported (39, 40). To balance the osmotic pressure, 750 mM sucrose was reconstituted inside, while the GUVs were collected in 750 mM glucose containing PBS buffer. DMSO-solubilized rapamycin (100 μ M) was administered in the outer GUV buffer to trigger translocation. For actin polymerization experiments, we reconstituted the components reported in Table 1.

Global rapamycin administration image acquisition

For CFP-FRB translocation experiments, we used an inverted epifluorescence microscope (Axiovert135TV, ZEISS) with 40 \times oil objective to track the CFP and mCherry signal intensity. For actin polymerization experiments, we used LSM780 confocal microscope (Zeiss) equipped with Plan-Aprochromat 63 \times /1.40 numerical aperture oil immersion differential interference contrast objective lens (Zeiss 420782-9900).

Image processing and biophysical parameters extraction

For Fig. 1 and fig. S1, MetaMorph software (Molecular Devices) was used to measure the average luminal and membrane fluorescence intensity for either CFP or mCherry. Values are reported after normalizing by the average intensities of each before rapamycin or DMSO treatment. All actin-containing microscopy data were analyzed using a custom MATLAB (MathWorks) script (Supplementary Materials and Image Processing Code). For preprocessing, image sequences were regionally cropped and smoothed with 2D median and Gaussian filtering. Individual GUVs were segmented on the basis of membrane marker signal (mCherry-FKBP-MARCKs) using intensity thresholding, morphological operations, and active contours technique.

Local rapamycin administration with a microinjector and image acquisition

The GUV content is listed in table S2. A 100- μ l droplet of freshly prepared GUVs was placed in a one-well Lab-Tek II chambered cover glass (Thermo Fisher Scientific) immediately before imaging. Local stimulation of GUVs was carried out by lowering a micropipette (Femtotips, Eppendorf) loaded with 10 μ l of a freshly prepared solution

of 500 μ M rapamycin and 100 μ M Alexa Fluor 647 dye (Thermo Fisher Scientific) and applying microinjection near GUVs of interest. The rapamycin-dye solution was rapidly prepared on ice in 100 μ l volume, diluted in double distilled H₂O from stock solutions of rapamycin (5 mM in 100% ethanol) and Alexa Fluor 647 (1 mM in DMSO). Concentrations were optimized on the basis of estimates of micropipette-generated chemical gradients under passive diffusion or forced flow (65) and considerations of needle clogging. The micropipette was then connected to a microinjector (Femtojet, Eppendorf) controlled by a micromanipulator (Eppendorf). Image acquisition began with the micropipette immersed in the liquid droplet but above the focal plane of GUVs, at an initial compensation pressure (P_c) of 5 to 10 hPa. To achieve local chemical dimerization, the micropipette was lowered near a GUV in the field of view, and compensation pressure was increased to between 30 and 50 hPa for a continuous local gradient. To relieve clogging and generate brief local gradients, microinjection pressures were also applied in bursts as needed [injection parameters: injection pressure (P_i) = 400 to 800 hPa; injection duration (t_i) = 5 to 10 s; P_c = 10 hPa]. Confocal image acquisition every 15 s was performed on LSM780 confocal laser-scanning microscope (Zeiss).

Reagents

Rabbit skeletal muscle actin (AKL99), pyrene-labeled actin (AP05), Arp2/3 complex (RP01P), and GST-WASP-VCA (VCG03-A) were purchased from Cytoskeleton. ATP for actin dialysis buffer was purchased from Gold Biotechnology. All lipids (table S1) were purchased from Avanti Polar Lipids. Hexadecane (H6703) and silicone oil [viscosity, 20 centistokes (25°C); 378348] were purchased from Sigma-Aldrich.

Statistical analysis

Symmetry breaking analysis from kymographs using correlation analysis and principal components analysis are detailed in the Supplementary Materials. To verify our method, we applied our analysis pipeline to a previously reported case of symmetry breaking in GUVs (fig. S16) (51). Please refer to the figure legends for the description of sample size and the corresponding statistical methods used.

Supplementary Materials

This PDF file includes:

- Supplementary Text
- Figs. S1 to S16
- Tables S1 and S2
- Legends for movies S1 to S3
- Legend for supplementary.xlsx file
- Legend for abaqus finite element analysis file
- DNA Sequence Files
- Raw Imaging Files
- Image Processing Code
- References

Other Supplementary Material for this manuscript includes the following:

- Movies S1 to S3
- Supplementary.xlsx File
- Abaqus Finite Element Analysis File

REFERENCES AND NOTES

1. D. J. Gross, The role of symmetry in fundamental physics. *Proc. Natl. Acad. Sci. U.S.A.* **93**, 14256–14259 (1996).
2. S. Katzir, The emergence of the principle of symmetry in physics. *Hist. Stud. Phys. Biol. Sci.* **35**, 35–65 (2004).

3. R. Li, B. Bowerman, Symmetry Breaking in Biology. *Cold Spring Harb. Perspect. Biol.* **2**, a003475 (2010).
4. S. Razavi, T. Inoue, Reconstitution of membrane symmetry breaking in *Plasma Membrane Shaping* (Elsevier, 2023), pp. 333–353.
5. T. D. Pollard, J. A. Cooper, Actin, a central player in cell shape and movement. *Science* **326**, 1208–1212 (2009).
6. K. Shilagardi, S. Li, F. Luo, F. Marikar, R. Duan, P. Jin, J. H. Kim, K. Murnen, E. H. Chen, Actin-propelled invasive membrane protrusions promote fusogenic protein engagement during cell-cell fusion. *Science* **340**, 359–363 (2013).
7. P. N. Devreotes, S. Bhattacharya, M. Edwards, P. A. Iglesias, T. Lampert, Y. Miao, Excitable signal transduction networks in directed cell migration. *Annu. Rev. Cell Dev. Biol.* **33**, 103–125 (2017).
8. T. Svitskina, The actin cytoskeleton and actin-based motility. *Cold Spring Harb. Perspect. Biol.* **2**, a018267 (2018).
9. N. Johnson, M. Krebs, R. Boudreau, G. Giorgi, M. LeGros, C. Larabell, Actin-filled nuclear invaginations indicate degree of cell de-differentiation. *Differentiation* **71**, 414–424 (2003).
10. C. Le Clainche, M. F. Carlier, Regulation of actin assembly associated with protrusion and adhesion in cell migration. *Physiol. Rev.* **88**, 489–513 (2008).
11. A. E. Carlsson, Membrane bending by actin polymerization. *Curr. Opin. Cell Biol.* **50**, 1–7 (2018).
12. S. Sawai, Y. Maeda, Y. Sawada, Spontaneous symmetry breaking turing-type pattern formation in a confined dictyostelium cell mass. *Phys. Rev. Lett.* **85**, 2212–2215 (2000).
13. S. M. Sears, M. Soljačić, D. N. Christodoulides, M. Segev, Pattern formation via symmetry breaking in nonlinear weakly correlated systems. *Phys. Rev. E* **65**, 036620 (2002).
14. I. Salazar-Ciudad, J. Jernvall, S. A. Newman, Mechanisms of pattern formation in development and evolution. *Development* **130**, 2027–2037 (2003).
15. J. Van Der Gucht, C. Sykes, Physical model of cellular symmetry breaking. *Cold Spring Harb. Perspect. Biol.* **1**, a001909 (2009).
16. N. H. Wubshet, B. Wu, S. Veerapaneni, A. P. Liu, Differential regulation of GUV mechanics via actin network architectures. *Biophys. J.* **122**, 2068–2081 (2023).
17. A. B. Goryachev, M. Leda, Many roads to symmetry breaking: Molecular mechanisms and theoretical models of yeast cell polarity. *Mol. Biol. Cell* **28**, 370–380 (2017).
18. R. Nussinov, C. J. Tsai, H. Jang, Are parallel proliferation pathways redundant? *Trends Biochem. Sci.* **45**, 554–563 (2020).
19. L. L. Pontani, J. Van Der Gucht, G. Salbreux, J. Heuvingh, J. F. Joanny, C. Sykes, Reconstitution of an actin cortex inside a liposome. *Biophys. J.* **96**, 192–198 (2009).
20. K. R. Levental, I. Levental, Giant plasma membrane vesicles: Models for understanding membrane organization. *Curr. Top. Membr.* **75**, 25–57 (2015).
21. M. Doktorova, F. A. Heberle, B. Eicher, R. F. Standaert, J. Katsaras, E. London, G. Pabst, D. Marquardt, Preparation of asymmetric phospholipid vesicles for use as cell membrane models. *Nat. Protoc.* **13**, 2086–2101 (2018).
22. J. Lemière, K. Carvalho, C. Sykes, Cell-sized liposomes that mimic cell motility and the cell cortex. *Methods Cell Biol.* **128**, 271–285 (2015).
23. A. P. Liu, D. L. Richmond, L. Maibaum, S. Pronk, P. L. Geissler, D. A. Fletcher, Membrane-induced bundling of actin filaments. *Nat. Phys.* **4**, 789–793 (2008).
24. K. Carvalho, J. Lemière, F. Faqir, J. Manzi, L. Blanchoin, J. Plastino, T. Betz, C. Sykes, Actin polymerization or myosin contraction: Two ways to build up cortical tension for symmetry breaking. *Philos. Trans. R. Soc. Lond. B Biol. Sci.* **310**, 16456–16461 (2013).
25. C. Simon, R. Kusters, V. Caorsi, A. Allard, M. Abou-Ghali, J. Manzi, A. Di Cicco, D. Lévy, M. Lenz, J. F. Joanny, C. Campillo, J. Plastino, P. Sens, C. Sykes, Actin dynamics drive cell-like membrane deformation. *Nat. Phys.* **15**, 602–609 (2019).
26. R. Lopes dos Santos, C. Campillo, Studying actin-induced cell shape changes using Giant Unilamellar Vesicles and reconstituted actin networks. *Biochem. Soc. Trans.* **50**, 1527–1539 (2022).
27. N. Ierushalmi, M. Malik-Garbi, A. Manhart, E. A. Shah, B. L. Goode, A. Mogilner, K. Keren, Centering and symmetry breaking in confined contracting actomyosin networks. *eLife* **9**, e55368 (2020).
28. T. Litschel, C. F. Kelley, D. Holz, M. Adeli Koudehi, S. K. Vogel, L. Burbaum, N. Mizuno, D. Vavylonis, P. Schwille, Reconstitution of contractile actomyosin rings in vesicles. *Nat. Commun.* **12**, 2254 (2021).
29. R. Sakamoto, M. Tanabe, T. Hiraiwa, K. Suzuki, S. Ishiwata, Y. T. Maeda, M. Miyazaki, Tug-of-war between actomyosin-driven antagonistic forces determines the positioning symmetry in cell-sized confinement. *Nat. Commun.* **11**, 3063 (2020).
30. Y. Bashirzadeh, H. Moghimianaval, A. P. Liu, Encapsulated actomyosin patterns drive cell-like membrane shape changes. *iScience* **25**, 104236 (2022).
31. L. Baldauf, F. Frey, M. Arribas Perez, T. Idema, G. H. Koenderink, Branched actin cortices reconstituted in vesicles sense membrane curvature. *Biophys. J.* **122**, 2311–2324 (2023).
32. N. A. Araújo, L. M. Janssen, T. Barois, G. Boffetta, I. Cohen, A. Corbetta, O. Dauchot, M. Dijkstra, W. M. Durham, A. Dussutour, S. Garnier, H. Gelderblom, R. Golestanian, L. Isa, G. H. Koenderink, H. Löwen, R. Metzler, M. Polin, C. P. Royall, A. Šarić, A. Sengupta, C. Sykes, V. Trianni, I. Tuval, N. Vogel, J. M. Yeomans, I. Zuriguel, A. Marin, G. Volpe, Steering self-organisation through confinement. *Soft Matter* **19**, 1695–1704 (2023).
33. N. H. Wubshet, A. P. Liu, Methods to mechanically perturb and characterize GUV-based minimal cell models. *Comput. Struct. Biotechnol. J.* **21**, 550–562 (2023).
34. J. Aguilar, T. Zhang, F. Qian, M. Kingsbury, B. McInroe, N. Mazouchova, C. Li, R. Maladen, C. Gong, M. Travers, R. L. Hatton, H. Choset, P. B. Umbanhowar, D. I. Goldman, A review on locomotion robophysics: The study of movement at the intersection of robotics, soft matter and dynamical systems. *Rep. Prog. Phys.* **79**, 110001 (2016).
35. R. Derose, T. Miyamoto, T. Inoue, Manipulating signaling at will: Chemically-inducible dimerization (CID) techniques resolve problems in cell biology. *Pflügers Arch.* **465**, 409–417 (2013).
36. C. B. Carbone, N. Kern, R. A. Fernandes, E. Hui, X. Su, K. C. Garcia, R. D. Vale, In vitro reconstitution of T cell receptor-mediated segregation of the CD45 phosphatase. *Proc. Natl. Acad. Sci. U.S.A.* **114**, E9338–E93458 (2017).
37. R. M. Caldwell, J. G. Bermudez, D. Thai, C. Aonbangkhen, B. S. Schuster, T. Courtney, A. Deiters, D. A. Hammer, D. M. Chenoweth, M. C. Good, Optochemical control of protein localization and activity within cell-like compartments. *Biochemistry* **57**, 2590–2596 (2018).
38. S. Pautot, B. J. Frisken, D. A. Weitz, Production of unilamellar vesicles using an inverted emulsion. *Langmuir* **19**, 2870–2879 (2003).
39. E. L. Meier, S. Razavi, T. Inoue, E. D. Goley, A novel membrane anchor for FtsZ is linked to cell wall hydrolysis in Caulobacter crescentus. *Mol. Microbiol.* **101**, 265–280 (2016).
40. S. Razavi, T. Inoue, D. N. Robinson, T. Luo, Methods for making giant vesicles and their use, US Patent 11,951,210 (2024).
41. Y. Zhang, H. Obuchi, T. Toyota, A practical guide to preparation and applications of giant unilamellar vesicles formed via centrifugation of water-in-oil emulsion droplets. *Membranes* **13**, 440 (2023).
42. T. Inobe, N. Nukina, Rapamycin-induced oligomer formation system of FRB-FKBP fusion proteins. *J. Biosci. Bioeng.* **122**, 40–46 (2016).
43. H. Nakamura, A. A. Lee, A. Sobhi Afshar, S. Watanabe, E. Rho, S. Razavi, A. Suarez, Y.-C. Lin, M. Tanigawa, B. Huang, R. DeRose, D. Bobb, W. Hong, S. B. Gabelli, J. Goutsias, T. Inoue, Intracellular production of hydrogels and synthetic RNA granules by multivalent molecular interactions. *Nat. Mater.* **17**, 79–89 (2018).
44. U. Dietrich, P. Krüger, T. Gutberlet, J. A. Käs, Interaction of the MARCKS peptide with PIP2 in phospholipid monolayers. *Biomembranes* **1788**, 1474–1481 (2009).
45. S. Razavi, S. Su, T. Inoue, Cellular signaling circuits interfaced with synthetic, post-translational, negating boolean logic devices. *ACS Synth. Biol.* **3**, 676–685 (2014).
46. T. P. Loisel, R. Boujemaa, D. Pantalon, M. F. Cartier, Reconstitution of actin-based motility of Listeria and Shigella using pure proteins. *Nature* **401**, 613–616 (1999).
47. M. F. Carlier, S. Wiesner, C. Le Clainche, D. Pantalon, Actin-based motility as a self-organized system: Mechanism and reconstitution in vitro. *C. R. Biol.* **326**, 161–170 (2003).
48. H. Nakamura, E. Rho, C. T. Lee, K. Itoh, D. Deng, S. Watanabe, S. Razavi, H. T. Matsabayashi, C. Zhu, E. Jung, P. Rangamani, S. Watanabe, T. Inoue, ActuAtor, a Listeria-inspired molecular tool for physical manipulation of intracellular organizations through de novo actin polymerization. *Cell Rep.* **42**, 113089 (2023).
49. I. Fujiwara, M. E. Zweifel, N. Courtemanche, T. D. Pollard, Latrunculin A accelerates actin filament depolymerization in addition to sequestering actin monomers. *Curr. Biol.* **28**, 3183–3192.e2 (2018).
50. S. Wiesner, E. Helfer, D. Didry, G. Ducouret, F. Lafuma, M. F. Carlier, D. Pantalon, A biomimetic motility assay provides insight into the mechanism of actin-based motility. *J. Cell Biol.* **160**, 387–398 (2003).
51. E. Abu Shah, K. Keren, Symmetry breaking in reconstituted actin cortices. *eLife* **3**, e01433 (2014).
52. H. Boukellal, O. Campás, J. F. Joanny, J. Prost, C. Sykes, Soft Listeria: Actin-based propulsion of liquid drops. *Phys. Rev. E Stat. Nonlin. Soft. Matter Phys.* **69**, 061906 (2004).
53. B. Lin, W. R. Holmes, C. J. Wang, T. Ueno, A. Harwell, L. Edelstein-Keshet, T. Inoue, A. Levchenko, Synthetic spatially graded Rac activation drives cell polarization and movement. *Proc. Natl. Acad. Sci. U.S.A.* **109**, E3668–E3677 (2012).
54. D. Scherfeld, N. Kahya, P. Schwille, Lipid dynamics and domain formation in model membranes composed of ternary mixtures of unsaturated and saturated phosphatidylcholines and cholesterol. *Biophys. J.* **85**, 3758–3768 (2003).
55. A. Otto, A. Otto, W. Just, G. Radons, Nonlinear dynamics of delay systems: An overview. *Phil. Trans. R. Soc. A* **377**, 20180389 (2019).
56. U. Hau, H. Hartmann, P. Trommler, A. A. Noegel, M. Schleicher, F-Actin capping by cap3234 requires heterodimeric conformation and can be inhibited with PIP2. *Biochem. Biophys. Res. Commun.* **181**, 833–839 (1991).
57. K. Dürre, F. C. Keber, P. Bleicher, F. Brauns, C. J. Cyron, J. Faix, A. R. Bausch, Capping protein-controlled actin polymerization shapes lipid membranes. *Nat. Commun.* **9**, 1630 (2018).
58. K. Y. Lee, S.-J. Park, K. A. Lee, S.-H. Kim, H. Kim, Y. Meroz, L. Mahadevan, K.-H. Jung, T. K. Ahn, K. K. Parker, K. Shin, Photosynthetic artificial organelles sustain and control ATP-dependent reactions in a protocellular system. *Nat. Biotechnol.* **36**, 530–535 (2018).
59. A. E. Carlsson, Growth velocities of branched actin networks. *Biophys. J.* **84**, 2907–2918 (2003).

60. B. Ding, H. Y. Narvaez-Ortiz, Y. Singh, G. M. Hocky, S. Chowdhury, B. J. Nolen, Structure of Arp2/3 complex at a branched actin filament junction resolved by single-particle cryo-electron microscopy. *Proc. Natl. Acad. Sci. U.S.A.* **119**, e2202723119 (2022).
61. T. Toyota, Y. Zhang, Identifying and manipulating giant vesicles: Review of recent approaches. *Micromachines* **13**, 644 (2022).
62. T. Tosaka, K. Kamiya, Function investigations and applications of membrane proteins on artificial lipid membranes. *Int. J. Mol. Sci.* **24**, 7231 (2023).
63. A. Caliari, M. M. Hanczy, M. Imai, J. Xu, T. Yomo, Quantification of giant unilamellar vesicle fusion products by high-throughput image analysis. *Int. J. Mol. Sci.* **24**, 8241 (2023).
64. L. van Buren, G. H. Koenderink, C. Martinez-Torres, DisGUVery: A versatile open-source software for high-throughput image analysis of giant unilamellar vesicles. *ACS Synth. Biol.* **12**, 120–135 (2023).
65. M. Postma, P. J. van Haastert, Mathematics of experimentally generated chemoattractant gradients. *Methods Mol. Biol.* **1407**, 381–396 (2016).
66. T. P. J. Knowles, M. J. Buehler, Nanomechanics of functional and pathological amyloid materials. *Nat. Nanotechnol.* **6**, 469–479 (2011).
67. F. Gittes, B. Mickey, J. Nettleton, J. Howard, Flexural rigidity of microtubules and actin filaments measured from thermal fluctuations in shape. *J. Cell Biol.* **120**, 923–934 (1993).
68. J. Zenker, M. D. White, M. Gasnier, Y. D. Alvarez, H. Y. G. Lim, S. Bissiere, M. Biro, N. Plachta, Expanding actin rings zipper the mouse embryo for blastocyst formation. *Cell* **173**, 776–791 (2018).
69. R. Kusters, C. Simon, R. Lopes Dos Santos, V. Caorsi, S. Wu, J.-F. Joanny, P. Sens, C. Sykes, Actin shells control buckling and wrinkling of biomembranes. *Soft Matter* **15**, 9647–9653 (2019).

Acknowledgments: We are grateful to J. Liu and E. Sandoval for force modeling insight; T. Luo for vesicle fabrication assistance; E. Rho for FRET data analysis aid; and C. Sykes, W. Timp, and R. Li for discussions. E. Goley supported FPLC and fluorimetry experiments, D. Raben provided lipid handling setup, and K. Kamiya and M. Tabuchi offered lipid membrane and GUV

fabrication advice. M. Kanemaki provided strep-tag plasmids, R. DeRose proofread the manuscript, and we appreciate C. Martinez-Torres group for sharing the DisGUVery image analysis pipeline. **Funding:** This work was supported by the National Institute of Health (R01GM123130, R01GM136858, and R35GM149329 to T.I.; R35GM128786 to B.C.; R01GM149073 to D.N.R. and P.A.I.; R01GM66817 to D.N.R.; and S10OD016374 to S. C. Kuo), the DoD DARPA (HR0011-16-C-0139 to P.A.I., D.N.R., and T.I.), the National Science Foundation (000819255 to T.I. and B.C.), and the PRESTO program of the Japan Science and Technology Agency (PRESTO, JPMJPR12A5 to T.I. and JPMJPR20KA to H.T.M.). S.R. was supported by the National Science Foundation and the Japan Society for the Promotion of Science (JSPS) East Asia and Pacific Summer Institutes and Johns Hopkins Lucille Elizabeth Hay graduate fellowships. **Author contributions:** S.R. and T.I. conceived the project. S.R. designed and performed the experiments and analyzed data. S.R. implemented the microinjector experiments with help from B.A.-S. F.W. performed modeling. B.A.-S. developed the image processing and statistical analysis pipeline with input from P.A.I., F.W., and S.R. H.T.M. performed the pyrene assay and purified and labeled actin with help from B.C. H.N. developed and characterized the ActA tool. N.T.H.N. performed the osmolarity measurements. P.A.I. helped with modeling. D.N.R. provided protein purification and GUV fabrication resources. S.R. and F.W. wrote the manuscript with help from T.I. and B.A.-S. All authors contributed to editing of the manuscript. **Competing interests:** S.R., T.I., and D.N.R. are inventors on a patent related to this work filed by the Johns Hopkins University (US Patent 11,951,210, filed on 12 December 2018 and published on 9 April 2024). The authors declare that they have no other competing interests. **Data and materials availability:** All data needed to evaluate the conclusions in the paper are present in the paper and/or the Supplementary Materials.

Submitted 20 September 2023

Accepted 8 May 2024

Published 12 June 2024

10.1126/sciadv.adk9731